JOURNAL OF COMPUTATIONAL PHYSICS **134,** 342–356 (1997)
ARTICLE NO. CP975712

Unsteady Simulation of Jets in a Cross Flow

Seonghyeon Hahn and Haecheon Choi

Department of Mechanical Engineering, Seoul National University, Seoul 151-742, Korea
E-mail: choi@socrates.snu.ac.kr

Received June 24, 1996; revised March 31, 1997

Effects of the computational time step and grid stretching on numerical solutions of a two-dimensional laminar boundary layer with a planar jet injected from a wall are investigated using a fully implicit time advancement scheme. A very large CFL number (CFL = 64) is determined for a time accurate solution, which provides a factor of 50 savings in the required CPU time as compared to a semi-implicit method. It is also noted that the grid stretching generates $2-\Delta$ waves in the flow investigated. A full three-dimensional numerical simulation has been performed to qualitatively investigate the interaction of jets in a turbulent cross flow using the direct numerical simulation technique. Turbulent vortex sheddings are observed behind jets and show a rapid diffusion in the downstream. It is also shown that a counter-rotating vortex pair existing in the downstream of the jet contributes an important role in the dynamics of the jet in a cross flow. © 1997 Academic Press

1. INTRODUCTION

Jets in a cross flow have a wide range of practical applications, such as the film cooling of turbine blades, VTOL aerodynamics, and chimney plumes of pollutants into atmosphere. Among these examples, improvements of the film-cooling effectiveness have been one of the most actively studied topics in turbomachinery during the last two decades. However, researches in this area so far have focused on the experimental measurement of the amount of heat transfer, without a close investigation of the underlying flow mechanism.

Although there have been some experimental attempts to supplement lack of understanding of the flow mechanism (see, for example, Yavuzkurt *et al.* [1], Andreopoulos and Rodi [2]), their experimental tools have shown an intrinsic limitation to make a complete description of the film-cooling flow field due to the highly turbulent and three-dimensional flow characteristics of film-cooling processes. Furthermore, an accurate prediction of the flow using the presently available Reynolds averaged turbulence models is hampered by the strong curvature of the streamline as well as the reversing flow (Leylek and Zerkle [3]). Therefore, more precise numerical tools such as direct numerical simulation or large eddy simulation techniques are now essential to gain knowledge of the interaction between the jet and cross flow and to develop a new film-cooling technology with a higher efficiency.

The full-scale simulation of turbulent flows occurred in film cooling, including the statistics of flow variables, nevertheless, requires an enormous computational resource mainly owing to the full three dimensionality and unsteadiness of the flow. On the other hand, a close examination of the basic computational parameters such as the grid resolution and the size of the computational time step is essential to achieve a successful result. Therefore, it is reasonable to explore the effect of these computational parameters on the computed flow field by investigating a rather simple and less time-consuming situation. A two-dimensional simulation of a planar jet in a laminar cross flow may be an appropriate candidate for this preliminary work because the unsteadiness and separation near the injection hole that occurred in film-cooling applications are also observed in a planar jet in a laminar cross flow, even though the inherent three-dimensional feature such as the horseshoe vortex does not exist in the two-dimensional jet. Moreover, this reduction to two-dimensional flow deserves to be investigated by itself in that information on the characteristics of the two-dimensional separation [4] may be provided.

Among the numerical parameters mentioned above, the determination of the largest time step, which allows a time-accurate solution, is most important because it is directly related to the computational cost. For example, Choi and Moin [5] determined the maximum computational time step of accurately predicting turbulence statistics in a channel flow and showed a factor of 5 savings in the required CPU time as compared to a semi-implicit method when the maximum time step was applied to a flow over riblets. In general, film cooling requires the magnitude of blowing on the wall to be an order of the free-stream speed. In this case, the computational time step is significantly restricted owing to the limitation of the Courant–Friedrichs–Lewy (CFL) number, when a semi-implicit method is adopted. Therefore, a fully implicit method is required to simulate unsteady flow of jets in a cross flow.

0021-9991/97 $25.00

In the present study, we investigate the effect of the computational time step on the computed two-dimensional flow field of a jet in a laminar cross flow using a fully implicit method and find a maximum computational time step for maintaining time accuracy. Based on the findings from this two-dimensional simulation, we simulate a fully three-dimensional flow field—circular jets in a turbulent cross flow—using the direct numerical simulation technique. Performing turbulent flow analysis using the direct numerical simulation technique requires an enormous computation time at the Reynolds number pursued in the experiment. Hence, as a first step, it is reasonable to consider rather a low Reynolds number flow. Our purpose is to examine complicated patterns of the flow in a film-cooling configuration, such as the separation bubble in front of the injection hole, the horseshoe vortex, vortex shedding, and kidney vortices at the downstream of the hole.

The numerical method used in this study is described in Section 2. Numerical results of a planar jet in a laminar cross flow with different computational time steps and grid spacings are presented in Section 3. The flow characteristics of jets in a turbulent cross flow is discussed in Section 4, followed by a summary in Section 5.

2. NUMERICAL METHOD

The governing equations for an incompressible flow are

$$\frac{\partial u_i}{\partial t} + \frac{\partial}{\partial x_j} u_i u_j = -\frac{\partial p}{\partial x_i} + \frac{1}{\mathrm{Re}} \frac{\partial}{\partial x_j} \frac{\partial u_i}{\partial x_j}, \tag{1}$$

$$\frac{\partial u_i}{\partial x_i} = 0, \tag{2}$$

where x_i are the Cartesian coordinates, and u_i are the corresponding velocity components. All variables are nondimensionalized by the inlet displacement thickness δ^* and the free-stream velocity u_∞, and Re is the Reynolds number, $\mathrm{Re} = u_\infty \delta^* / \nu$, where ν is the kinematic viscosity.

The time integration method used to solve Eqs. (1) and (2) is based on a fully implicit, fractional step method [5]; all terms in Eq. (1) are advanced with the Crank–Nicolson method in time. A four-step time advancement scheme for Eqs. (1) and (2) is

$$\frac{\hat{u}_i - u_i^n}{\Delta t} + \frac{1}{2} \frac{\partial}{\partial x_j} (\hat{u}_i \hat{u}_j + u_i^n u_j^n) = -\frac{\partial p^n}{\partial x_i} + \frac{1}{2\mathrm{Re}} \frac{\partial}{\partial x_j} \frac{\partial}{\partial x_j} (\hat{u}_i + u_i^n), \tag{3}$$

$$\frac{u_i^* - \hat{u}_i}{\Delta t} = \frac{\partial p^n}{\partial x_i}, \tag{4}$$

$$\frac{\partial}{\partial x_i} \frac{\partial p^{n+1}}{\partial x_i} = \frac{1}{\Delta t} \frac{\partial u_i^*}{\partial x_i}, \tag{5}$$

$$\frac{u_i^{n+1} - u_i^*}{\Delta t} = -\frac{\partial p^{n+1}}{\partial x_i}, \tag{6}$$

where Δt is the computational time step. Implicit treatment of the convective and viscous terms eliminates the numerical stability restriction. By substituting Eqs. (4) and (6) into Eq. (3), one can easily show that the overall accuracy of the splitting scheme is second order. Note that the implicit treatment of the convection term requires one more step (Eq. (4)) as compared to the semi-implicit method (see Kim and Moin [6]).

A Newton–iterative method is used to solve the nonlinear momentum equation (3). Rearranging Eq. (3) gives

$$F_i(\hat{\mathbf{u}}) \equiv \hat{u}_i + \frac{\Delta t}{2} \left(\frac{\partial}{\partial x_j} \hat{u}_i \hat{u}_j - \frac{1}{\mathrm{Re}} \frac{\partial}{\partial x_j} \frac{\partial}{\partial x_j} \hat{u}_i \right) - R_i(\mathbf{u}^n, p^n) = 0, \tag{7}$$

where

$$R_i(\mathbf{u}^n, p^n) = u_i^n + \frac{\Delta t}{2} \left(-2 \frac{\partial p^n}{\partial x_i} - \frac{\partial}{\partial x_j} u_i^n u_j^n + \frac{1}{\mathrm{Re}} \frac{\partial}{\partial x_j} \frac{\partial}{\partial x_j} u_i^n \right). \tag{8}$$

Application of a Newton–iterative method provides

$$\left(\frac{\mathscr{D} F_i}{\mathscr{D} \hat{u}_j} \right)^k \delta \hat{u}_j = \delta \hat{u}_i + \frac{\Delta t}{2} \frac{\partial}{\partial x_j} (\hat{u}_i^k \delta \hat{u}_j + \hat{u}_j^k \delta \hat{u}_i) - \frac{\Delta t}{2\mathrm{Re}} \frac{\partial}{\partial x_j} \frac{\partial}{\partial x_j} \delta \hat{u}_i = -F_i^k, \tag{9}$$

where $\delta \hat{u}_j = \hat{u}_j^{k+1} - \hat{u}_j^k$ and k is the iteration index.

Using the approximating factorization scheme [7], Eq. (9) is formulated as

$$\left(1 + \frac{\Delta t}{2} \frac{\partial}{\partial x_j} \hat{u}_j^k - \frac{\Delta t}{2\mathrm{Re}} \frac{\partial}{\partial x_j} \frac{\partial}{\partial x_j} \right) \delta \hat{u}_i = -F_i^k - \frac{\Delta t}{2} \frac{\partial}{\partial x_j} \hat{u}_i^k \delta \hat{u}_j$$
$$\prod_{\alpha=1}^{3} \left(1 + \frac{\Delta t}{2} \frac{\partial}{\partial x_\alpha} \hat{u}_\alpha^k - \frac{\Delta t}{2\mathrm{Re}} \frac{\partial^2}{\partial x_\alpha^2} \right) \delta \hat{u}_i \approx -F_i^k - \frac{\Delta t}{2} \frac{\partial}{\partial x_j} \hat{u}_i^k \delta \hat{u}_j. \tag{10}$$

Equation (10) is solved with a tridiagonal matrix inversion. When converged ($\delta \hat{u}_i = 0$), the original nonlinear equation (3) is satisfied.

All the spatial derivatives are resolved with the second-order central-difference scheme using a staggered mesh

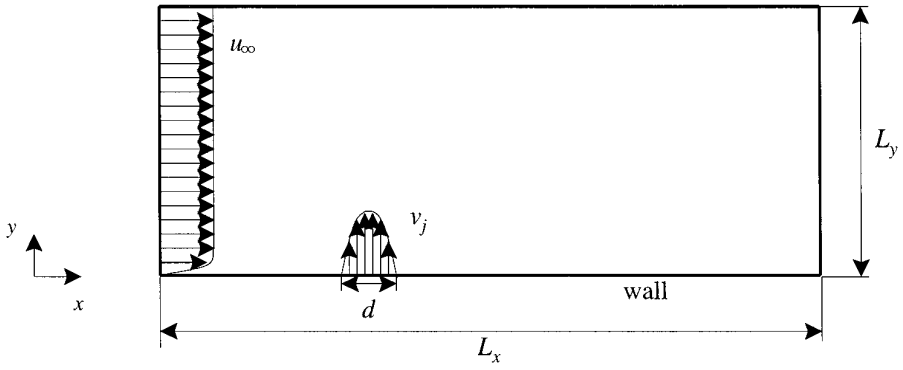

FIG. 1. Schematic diagram of the flow field.

system. The continuity equation is satisfied through the solution of a Poisson equation (5). In this paper, we use u, v, and w to denote the velocity components in the streamwise (x), wall-normal (y), and spanwise (z) directions, respectively.

The CFL number is defined as

$$\mathrm{CFL} = \max\left(\frac{|u|\,\Delta t}{\Delta x} + \frac{|v|\,\Delta t}{\Delta y} + \frac{|w|\,\Delta t}{\Delta z}\right), \qquad (11)$$

where Δx, Δy, and Δz denote the grid spacings in the streamwise, wall-normal, and spanwise directions, respectively.

3. A PLANAR JET IN A LAMINAR CROSS FLOW

As a preliminary study toward fully three-dimensional unsteady simulation of jets in a turbulent cross flow, a two-dimensional unsteady simulation of a planar jet in a laminar cross flow is performed in order to investigate the effects of the computational time step and grid stretching on the computed flow field.

3.1. *Computational Details*

The flow geometry and coordinate system are shown in Fig. 1. The computational domain of the present study is $183.8\delta^* < x < 314.7\delta^*$ and $0 < y < 60\delta^*$. Note that δ^* is the displacement thickness in an unperturbed laminar flat plate boundary layer. The Reynolds number at the inlet is $\mathrm{Re} = u_\infty\delta^*/\nu = 544.17$. This corresponds to the Reynolds number of 10^5 based on the streamwise distance from the leading edge of a flat plate. The injection slot has the width of $d = 5.2\delta^*$ and its upstream edge is located $4.8d$ downstream from the inlet ($x = 208.9\delta^*$). The Reynolds number at the slot is $\mathrm{Re}_x = u_\infty x/\nu = 1.14 \times 10^5$ ($\mathrm{Re} = u_\infty\delta^*/\nu = 580.1$). This Reynolds number is very close to transitional Reynolds numbers so that a three-dimensional flow evolution might occur in the presence of finite amplitude disturbances. However, the main motivation of choosing this relatively high Reynolds number is that we are aiming for a direct numerical simulation of jets in a cross flow at a similar Reynolds number (see Section 4). Numerical issues occurred from the simulation of jets in a cross flow are discussed in detail in Sections 3.2 and 3.3 with the present simplified two-dimensional flow model, which is nearly impossible with fully three-dimensional computations.

The grid points used are 577×181 in the x and y directions, respectively. About 100 grid points are located inside the boundary layer thickness using a hyperbolic tangent distribution. Twenty six grids are uniformly distributed inside the slot and the grid stretching factor used in the upstream from the injection slot is 1.038. In the direction downstream from the slot, three different stretching factors (r = 1, 1.005, and 1.01) are used in order to investigate the effect of the stretching factor on the computed flow field. It is well known that large stretching factors result in $2 - \Delta$ waves (wiggles) in the computed result [8–10]. We have also simulated two more grids, 897×271 and 1155×361. The computed Strouhal numbers changed by less than 1% in both cases.

A laminar boundary layer velocity profile is imposed at the inlet. A convective outflow boundary condition, $\partial u_i/\partial t + c\partial u_i/\partial x = 0$, is used at the outlet, which allows the propagating vortex structure to exit the domain with minimum distortion. In the present study, c is taken to be an average exit velocity [4]. A no-slip boundary condition is imposed at the solid wall. At the injection slot, a parabolic velocity profile is imposed to simulate a laminar jet. The volume-averaged velocity of the jet ($\bar{v}_j$) is half of the free-stream velocity, $\bar{v}_j = 0.5u_\infty$. At the far-field boundary, $u = u_\infty$ and $\partial v/\partial y = 0$ are used. This condition is valid only when the height of the computational domain is sufficiently large. The current height of the computational domain, $L_y = 60\delta^*$, has been determined from a prior investigation of the influence of a jet on the far-field boundary.

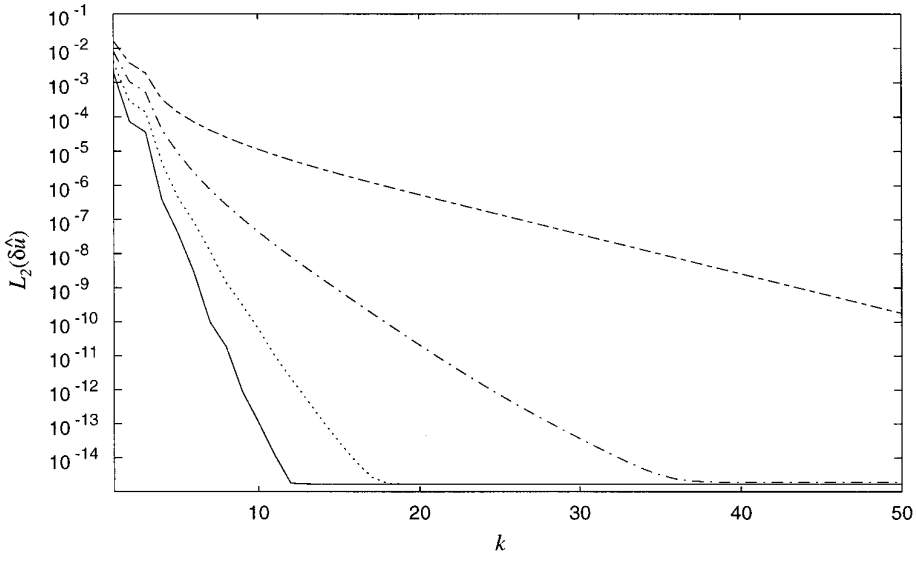

FIG. 2. Convergence histories of the Newton–iterative scheme: ———, CFL = 32; · · ·, CFL = 64; –·–, CFL = 128; –––, CFL = 256. $L_2(\delta\hat{u})$ denotes the L_2 norm of $\delta\hat{u}$.

3.2. *CFL Number*

Four different CFL numbers, CFL = 32, 64, 128, and 256, are investigated in this study. Those CFL numbers correspond to the computational time steps, $\Delta tu_\infty/\delta^* = 0.055$, 0.11, 0.22, and 0.44, respectively. Figure 2 shows the Newton–iteration convergence with respect to the CFL number. It is seen that a slow convergence is obtained for larger CFL numbers. Note that the CFL numbers used in this study are very large compared to those used in usual boundary layer computations. In the case of CFL = 64, five to six iterations of Eq. (10) are required to satisfy the convergence criterion of 10^{-7} and about 6% of the CPU time is needed in one Newton iteration per each time step. Considering that a semi-implicit time advancement imposes the restriction of CFL $\sim$ 1 owing to the numerical stability, a fully implicit time integration with CFL = 64 achieves about a factor of 50 savings in the required CPU time as compared to a semi-implicit method, while maintaining time accuracy (see below).

A Blasius boundary layer solution was first imposed on the computational domain at $tu_\infty/\delta^* = 0$ and the jet injection was applied from $tu_\infty/\delta^* = 0$. Figure 3 shows time histories of the streamwise velocity measured at four different locations downstream from the jet slot, where CFL = 64 is used. A periodic behavior with a constant frequency is shown after an initially developing period.

The effect of the CFL number on the computed flow is investigated. The initial flow field used for this test is the solution at $tu_\infty/\delta^* = 700$ with CFL = 64 (Fig. 3). Figure 4 shows time histories of the streamwise velocity for four different CFL numbers. Note that the results of CFL = 32 and 64 are almost identical, while small-scale motions are not accurately predicted as the computational time step becomes larger. Therefore, it can be said that the numerical solution with CFL = 64 is a time-accurate solution. It is also interesting to note that each case shows a periodic behavior. The computed Strouhal numbers are $St_{\delta^*} = f\delta^*/u_\infty = 0.0209$, 0.0209, 0.0210, and 0.0212 at CFL = 32, 64, 128, and 256, respectively, where f is the frequency. The Strouhal numbers show differences by less than 1.5%. It is clear from Fig. 4 that $\Delta tu_\infty/\delta^* = 0.11$ (CFL = 64) corresponds to the maximum time step which permits the time-accurate solution. Considering that the semi-implicit time advancement imposes the restriction of CFL $\sim$ 1 owing to the numerical stability, it can be said that a fully implicit time advancement is essentially required in unsteady simulation of jets in a cross flow.

The mean reattachment length and root-mean-square variables were also computed for the CFL numbers investigated in the present study. The mean reattachment lengths showed no difference for all the cases, while the root-mean-square variables showed some differences in the cases of CFL = 128 and 256. The velocity fluctuations showed about 6% and 10% discrepancies at CFL = 128 and 256, respectively, when compared with those at CFL = 32 and 64.

Figure 5 shows trajectories of the vortices as a function of time. The vortex centers are detected from local minima of the pressure [11]. The propagating speed of the vortices becomes larger as they move downstream of the jet. Also, a larger propagating speed is obtained at CFL = 256, but the

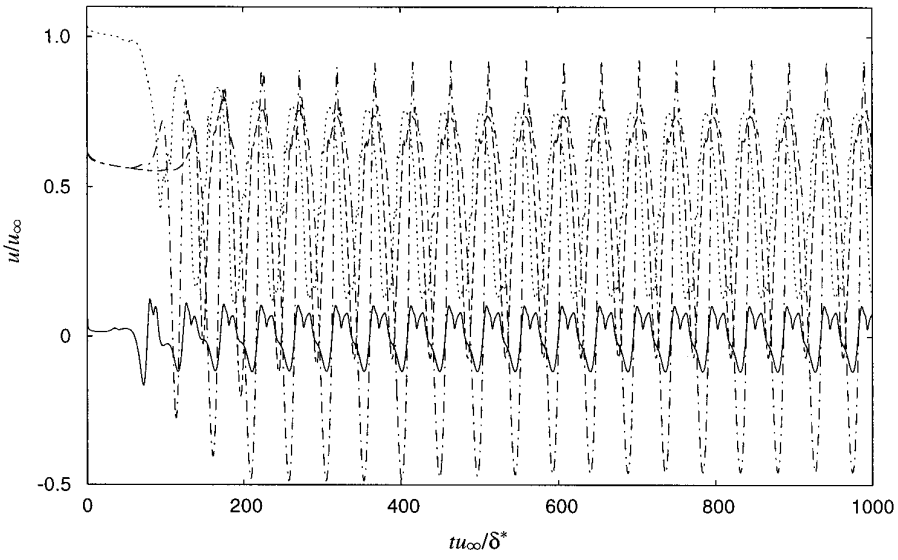

FIG. 3. Time histories of the streamwise velocity (CFL = 64): ———, $y = 0.027\delta^*$ at the $5d$ location downstream from the jet slot; · · ·, $y = 4.59\delta^*$ at the $7.5d$ location downstream from the jet slot; – · –, $y = 1.04\delta^*$ at the $10d$ location downstream from the jet slot; – – –, $y = 1.04\delta^*$ at the $15d$ location downstream from the jet slot.

difference is very small. Trajectories of the vortices are nearly the same in the cases of CFL = 32 and 64 and some differences are observed in the cases of CFL = 128 and 256.

Figure 6 shows contours of the local CFL number $(=|u|\,\Delta t/\Delta x + |v|\,\Delta t/\Delta y)$ at an instantaneous flow field obtained from the simulation with CFL = 64, where $\Delta t = 0.11\delta^*/u_\infty$. This figure clearly shows the reason that the time-accurate solution is possible with a very large CFL number: Because of the large wall-normal velocity of the jet $(\sim O(u_\infty))$ and the dense grid clustering near the wall (small Δy), large local CFL numbers are observed very near the injection slot. Although there exist very large local CFL numbers in the vicinity of the slot, the entire flow field still shows CFL ≤ 1, implying that the large CFL number used in this study is only for overcoming the numerical difficulties that occurred near the jet slot. Therefore, it can be postulated that a larger blowing ratio $(\overline{v}_j/u_\infty)$ will further restrict the size of the computational time step when a semi-implicit method is used, while in the case of a fully implicit method a larger CFL number results in a time-accurate solution.

Figure 7 shows the temporal evolution of the vorticity field during about one period in the limit cycle using CFL = 64. The mechanism of vortex shedding by the jet injection is clearly shown in this figure; a vortex (negative vorticity) generated from the interaction of the jet and boundary layer flow travels in the downstream and causes a vorticity with an opposite sign in the vicinity of the wall due to the no-slip condition on the wall. This positive vorticity (secondary vortex) is lifted up by the primary vortex and then the secondary vortex plays the role of cutting off the main vortex from the jet exit.

3.3. *Grid Stretching*

Central difference schemes suffer from the emergence of grid-to-grid oscillations ($2-\Delta$ waves, wiggles) when used for high Reynolds number simulations. Several sources for $2-\Delta$ waves have been identified by Gresho and Lee [8]. One of the main sources of $2-\Delta$ waves is the grid stretching. In the present study, we investigate the effect of the grid stretching on the computed flow using three different stretching factors, $r = 1$, 1.005, 1.01. For all three cases, the minimum and maximum of the grid sizes in the upstream of the jet slot are fixed: i.e., $\Delta x_{\min} = 0.2\delta^*$, $\Delta x_{\max} = 1.1105\delta^*$, $\Delta y_{\min} = 0.00128\delta^*$, and $\Delta y_{\max} = 1.4\delta^*$. On the other hand, in the downstream of the jet slot, the minimum grid size is the same, $\Delta x_{\min} = 0.2\delta^*$, but the maximum grid sizes are different, $\Delta x = 0.2\delta^*$ (uniform) for $r = 1$, $\Delta x_{\max} = 0.6822\delta^*$ for $r = 1.005$, and $\Delta x_{\max} = 1.223\delta^*$ for $r = 1.01$, respectively.

Figure 8 shows contours of the wall-normal velocity at a given time $(tu_\infty/\delta^* = 550)$. An instantaneous flow field with a dense uniform mesh (577×181) is clearly wiggle-free, while flow fields with $r = 1.005$ and 1.01 show $2-\Delta$ waves in the downstream of the jet slot. It is also shown that the propagating speed of the primary vortices is slightly affected by the grid stretching factor. It is surprising to note that the stretching factor is very limited for wiggle-free solutions in the flow investigated in this study. As

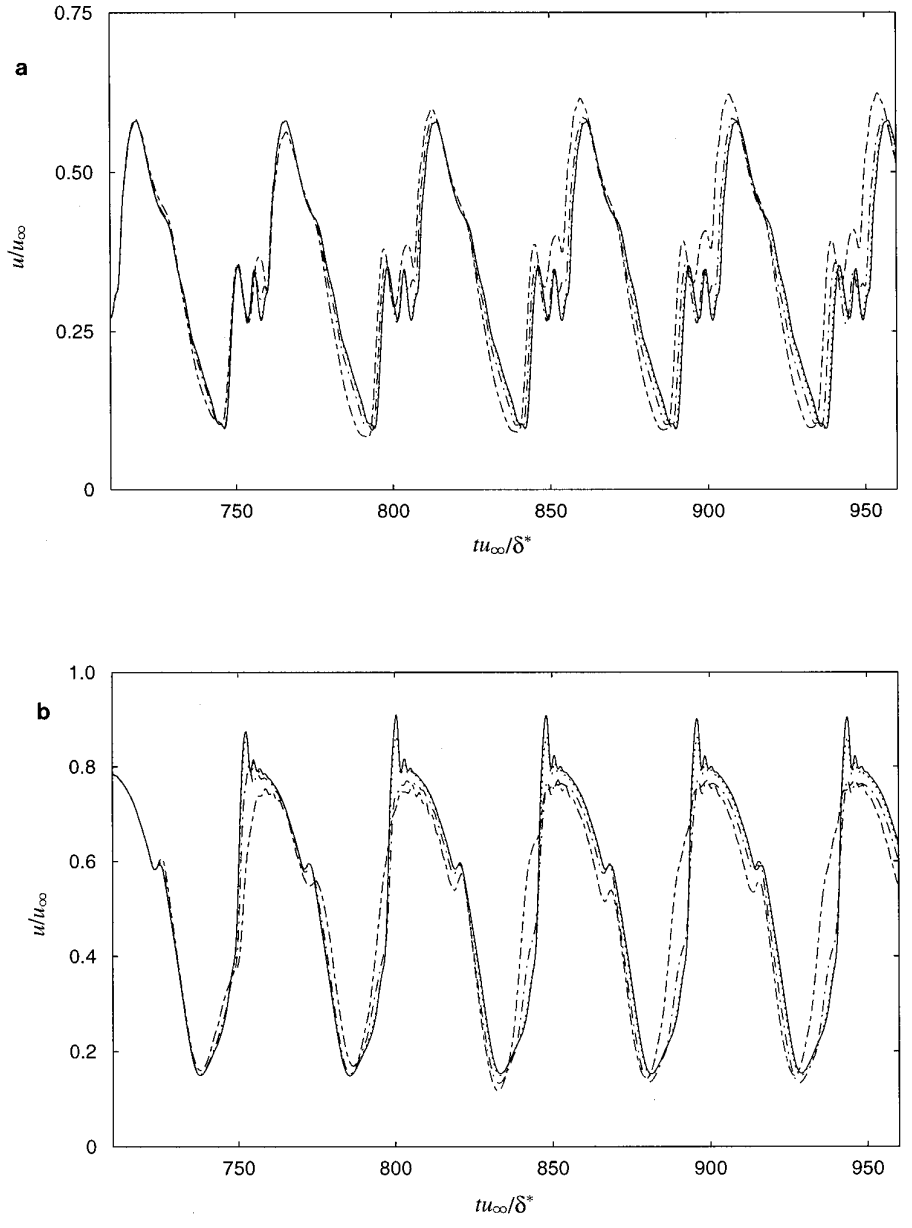

FIG. 4. Time histories of the streamwise velocities with CFL = 32 (———); 64 (· · ·); 128 (– · –); and 256 (– – –). (a) $y = 4.59\delta^*$ at the $5d$ location downstream from the jet slot; (b) $y = 4.59\delta^*$ at the $10d$ location downstream from the jet slot.

shown by Cain and Bush [10], waves propagating into an increasingly coarse mesh are amplified in a centered scheme. Figure 8d shows a solution obtained from a coarse uniform mesh. The resolution is half the mesh used in Fig. 8a. The solution is nearly wiggle-free, but it does not predict the propagating speed correctly.

High-order upwinding schemes such as QUICK [12] or Rai and Moin's fifth-order upwind-biased method [13] may not produce $2 - \Delta$ wiggles in the presence of the grid stretching. Those schemes can be implemented within the frame of the fully implicit method with the expense of a wider band-width-matrix inversion.

4. CIRCULAR JETS IN A TURBULENT CROSS FLOW

In this section, a fully three-dimensional unsteady simulation of jets in a turbulent cross flow is performed using the direct numerical simulation technique, based on the findings from Section 3. Our purpose is to examine complicated patterns of the flow in a film-cooling configuration,

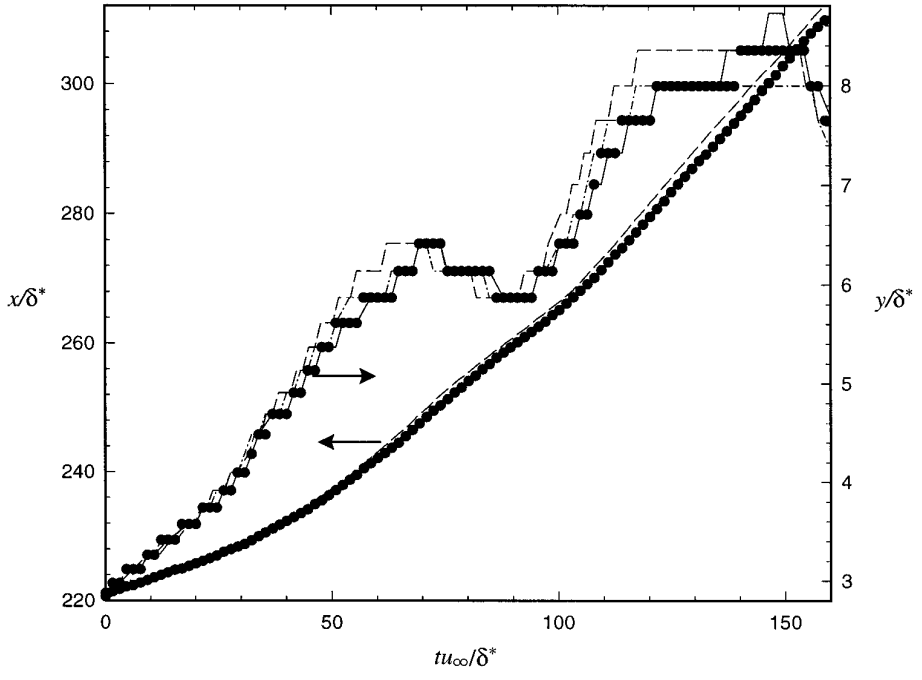

FIG. 5. Trajectories of the vortex center detected from local minima of the pressure: ———, CFL = 32; ●, CFL = 64; – · –, CFL = 128; – – –, CFL = 256. See also Fig. 7.

such as the separation bubble in front of the injection hole, the horseshoe vortex, vortex shedding, and kidney vortices downstream of the hole.

4.1. *Computational Details*

A schematic diagram of the computational domain is shown in Fig. 9. The computational domain size of the present study is $L_x = 275\delta^*_{in}$, $L_y = 40\delta^*_{in}$, and $L_z = 25\delta^*_{in}$, where δ^*_{in} is the displacement thickness at the inlet turbulent boundary layer. In this computational domain, we have set up a grid system of $705 \times 161 \times 129$ grid points in the streamwise, wall-normal, and spanwise directions, respectively. In the wall-normal direction, about 115 grid points are clustered inside the boundary layer thickness, and uniform grids are used in the streamwise and spanwise directions. The present mesh has been determined from

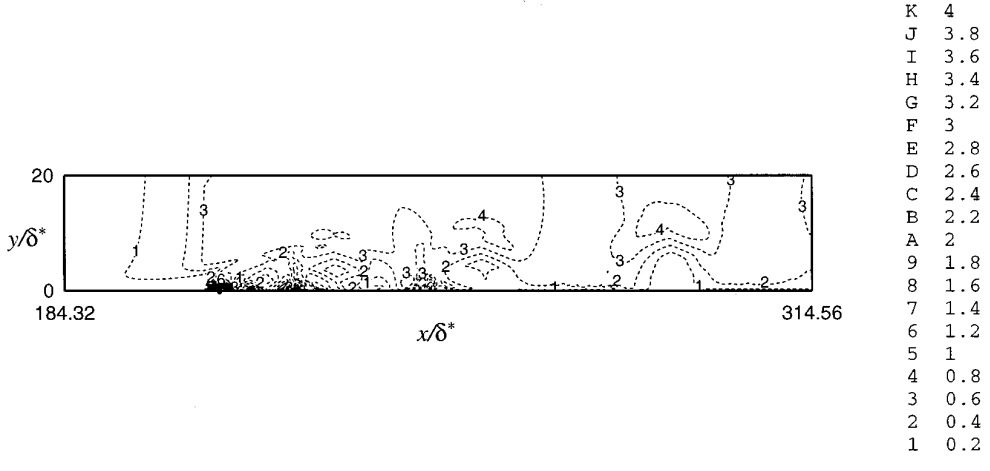

FIG. 6. Contours of the local CFL number ($=|u|\ \Delta t/\Delta x + |v|\ \Delta t/\Delta y$) at $tu_\infty/\delta^* = 960$ (CFL = 64): ———, local CFL > 1; ---, local CFL ≤ 1; ●, local CFL = 64.

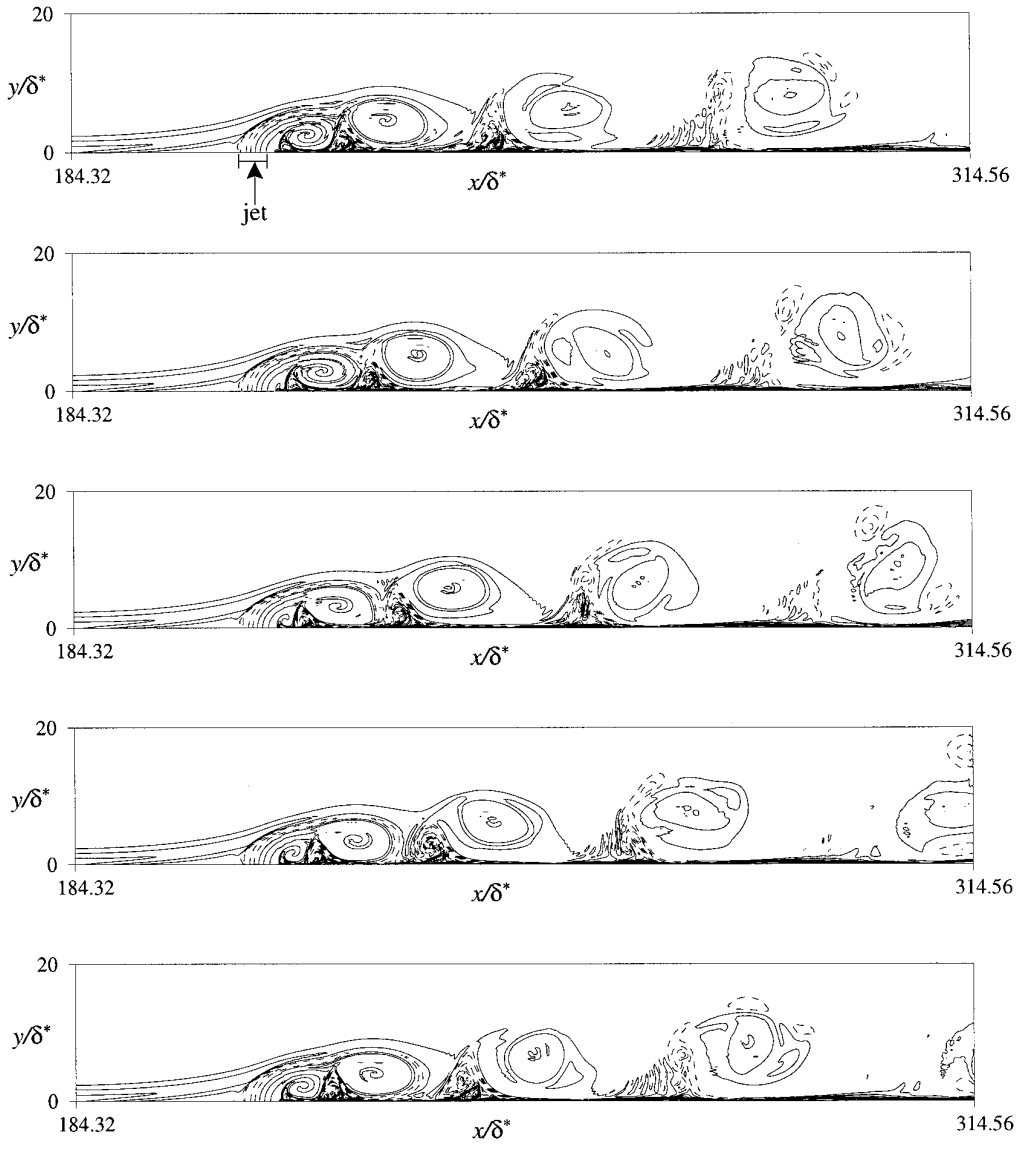

FIG. 7. Time sequence of the evolution of vortices from $tu_\infty/\delta^* = 910$ to 950 with increments of 10 (CFL = 64). Contour levels normalized by u_∞ and δ^* are from -2.1 to 1.9 by increments of 0.2. Positive contours of the spanwise vorticity are dashed.

an extensive resolution study. At the present mesh system, no wiggles have been found at instantaneous flow fields. The non-dimensional grid spacings based on the wall units are $\Delta x^+ = 10.6$, $\Delta y^+_{\min} = 0.023$, $\Delta y^+_{\max} = 25$, and $\Delta z^+ = 5.3$.

The width of the injection hole is $d = 7\delta^*_{\text{in}}$ and the hole is located 135 δ^*_{in} ($\approx 19d$) downstream of the inlet, which guarantees a fully developed turbulent boundary layer flow upstream of the hole (see below). Eighteen and 36 uniform grids are located inside this hole in the streamwise and spanwise directions, respectively. The computational domain length from the hole to the flow exit is about $19d$.

The inlet Reynolds number based on the displacement thickness and free-stream velocity is 500 [14]. This Reynolds number is very small compared to that of experimental studies (see, for example, [2]). Performing turbulent flow analysis using the direct numerical simulation technique requires an enormous computation time at the Reynolds number pursued in the experiment. Hence, as a first step, it is reasonable to consider rather a low Reynolds number flow. Even though it is not possible to quantitatively compare the present results with those of experimental studies due to the difference of the Reynolds numbers investigated, we believe that the essential features seen at high Reynolds numbers should appear in the present computation.

The inflow boundary condition is based on the method

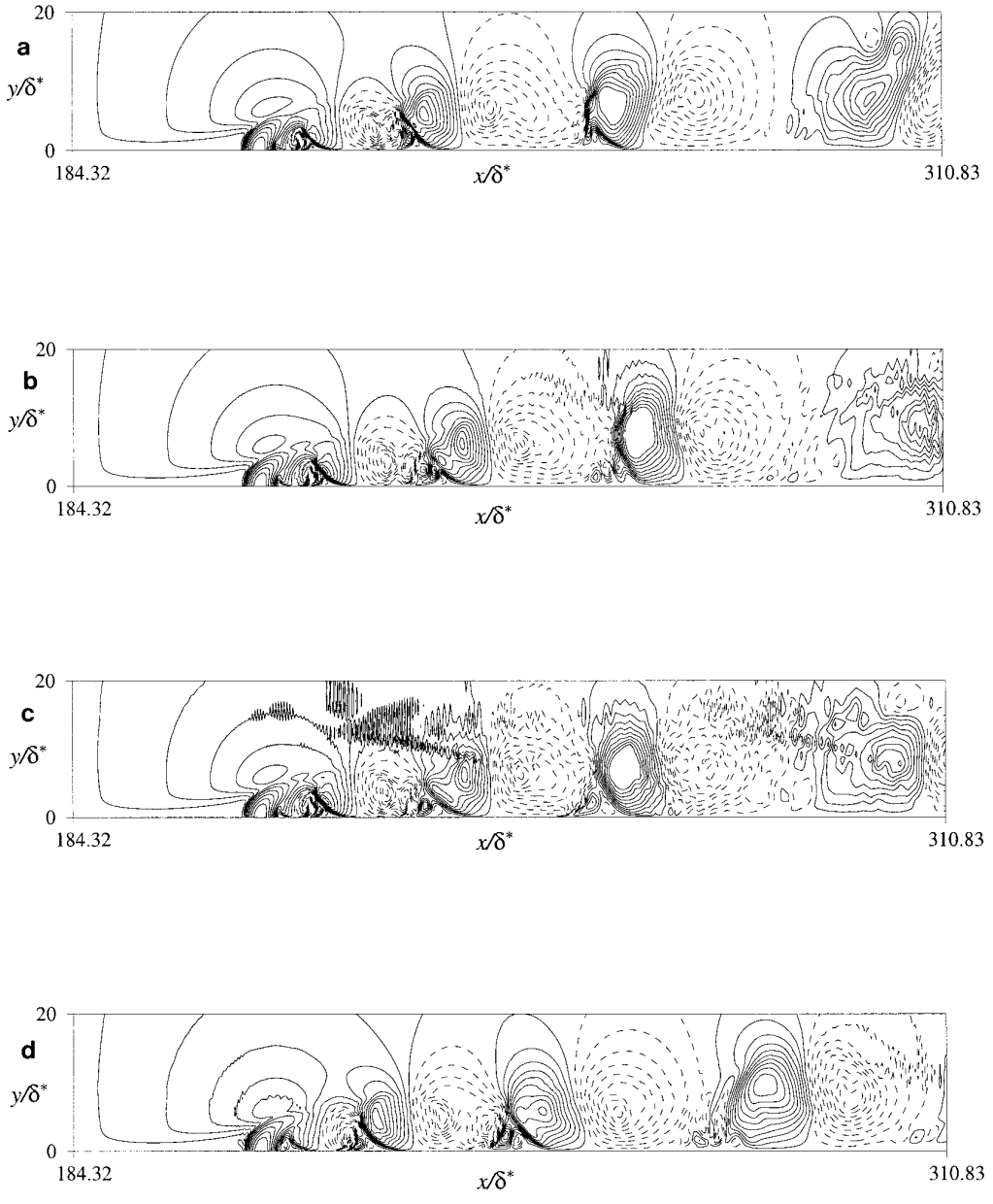

FIG. 8. Effect of the grid stretching on the computed flow: (a) $r = 1$ (dense uniform grid); (b) $r = 1.005$; (c) $r = 1.01$; (d) $r = 1$ (coarse uniform grid; half resolution of (a)), where r denotes the grid stretching factor downstream from the jet slot. Shown are contours of the wall-normal velocity at $tu_\infty/\delta^* = 550$.

by Na and Moin [15], where they applied amplitude jittering on the fluctuation components of Spalart's database [14]. A transition length of $l = 120\delta^*_{\text{in}}$ from the artificial flow inlet was necessary to recover a fully developed turbulent boundary layer flow at the upstream of the hole (Fig. 10).

The no-slip condition is imposed on the wall and a convective outflow boundary condition, $\partial u_i/\partial t + c\partial u_i/\partial x = 0$, is imposed at the outlet, where c denotes the convection velocity [4]. A periodic boundary condition is imposed in the spanwise direction, which determines the spacing between jet holes in the spanwise direction. At the injection hole, a parabolic velocity profile with a volume-average velocity $\overline{v}_j/u_\infty = 0.5$ is imposed. At the far-field, the boundary conditions, $u = u_\infty$ and $\partial v/\partial y = \partial w/\partial y = 0$, are used.

The computational time step used is $\Delta t = 0.2\delta^*_{\text{in}}/u_\infty$ ($\Delta t^+ = 0.28$). The computational time step smaller than $\Delta t^+ = 0.4$ provided an accurate prediction of turbulence statistics in wall-bounded flow (see [5]). At this time step, the CFL number is about 200 for the mesh used in the

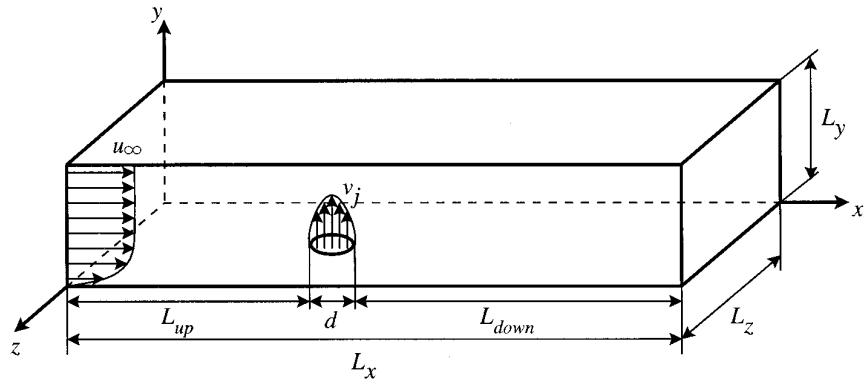

FIG. 9. Schematic diagram of the flow field.

present study. An accurate prediction of flow fields with such a high CFL number was provided in Section 3.

The CPU time required to simulate the flow is about 300 CRAY YMP C90 seconds per time step and the core memory needed is 350 MW. About 2000 time steps are required for integrating one flow-through time interval.

4.2. *Results*

Figure 11 shows a time sequence of the velocity vector in the center plane (x, y). A separating flow region is observed in front of the hole, which is due to the adverse pressure gradient generated from the injection. It is also seen from Fig. 11 that a significant flow modification occurs up to $y = 10\delta^*_{in}$ at the downstream. A strong vortex is created behind the jet and then it creates a reverse flow there. This vortex travels in the downstream but diffuses very quickly due to strong turbulent motion, which is quite different from the observation of two-dimensional flow in Section 3.

Figure 12 shows the velocity vector in the (x, z) planes. Flow features look very similar to the flow behind a circular cylinder. That is, there is a clear vortex shedding behind a jet. Therefore, the reverse flow shown in Fig. 11 is a fully three-dimensional phenomenon. Again, the vortex diffuses very rapidly in the downstream.

Contours of the wall pressure and streamwise velocity very near the wall are shown in Fig. 13. An adverse strong pressure gradient is developed in front of the jet, causing a separation. Streaky structures in a fully developed turbulent boundary layer are shown in the upstream of the hole.

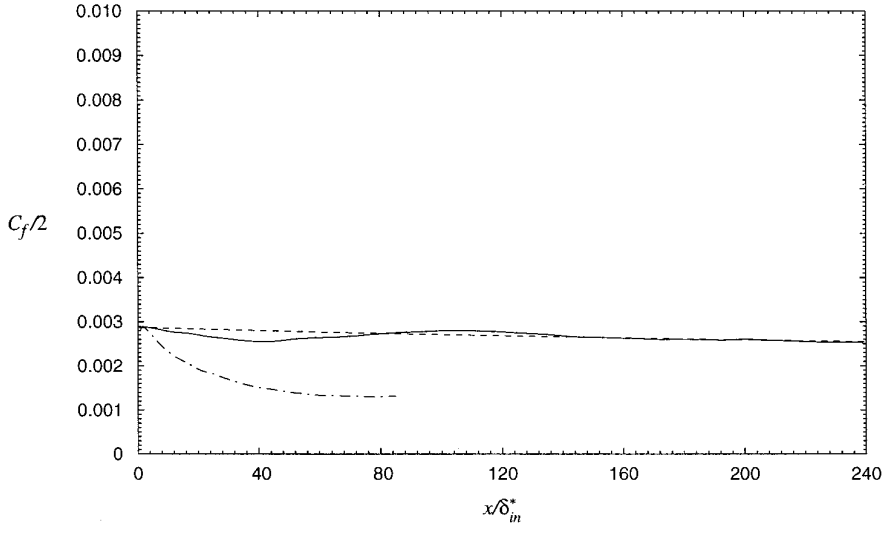

FIG. 10. The skin-friction coefficient in a turbulent boundary layer: ———, present study; – · –, random phase method [16]; ---, power-law assumption.

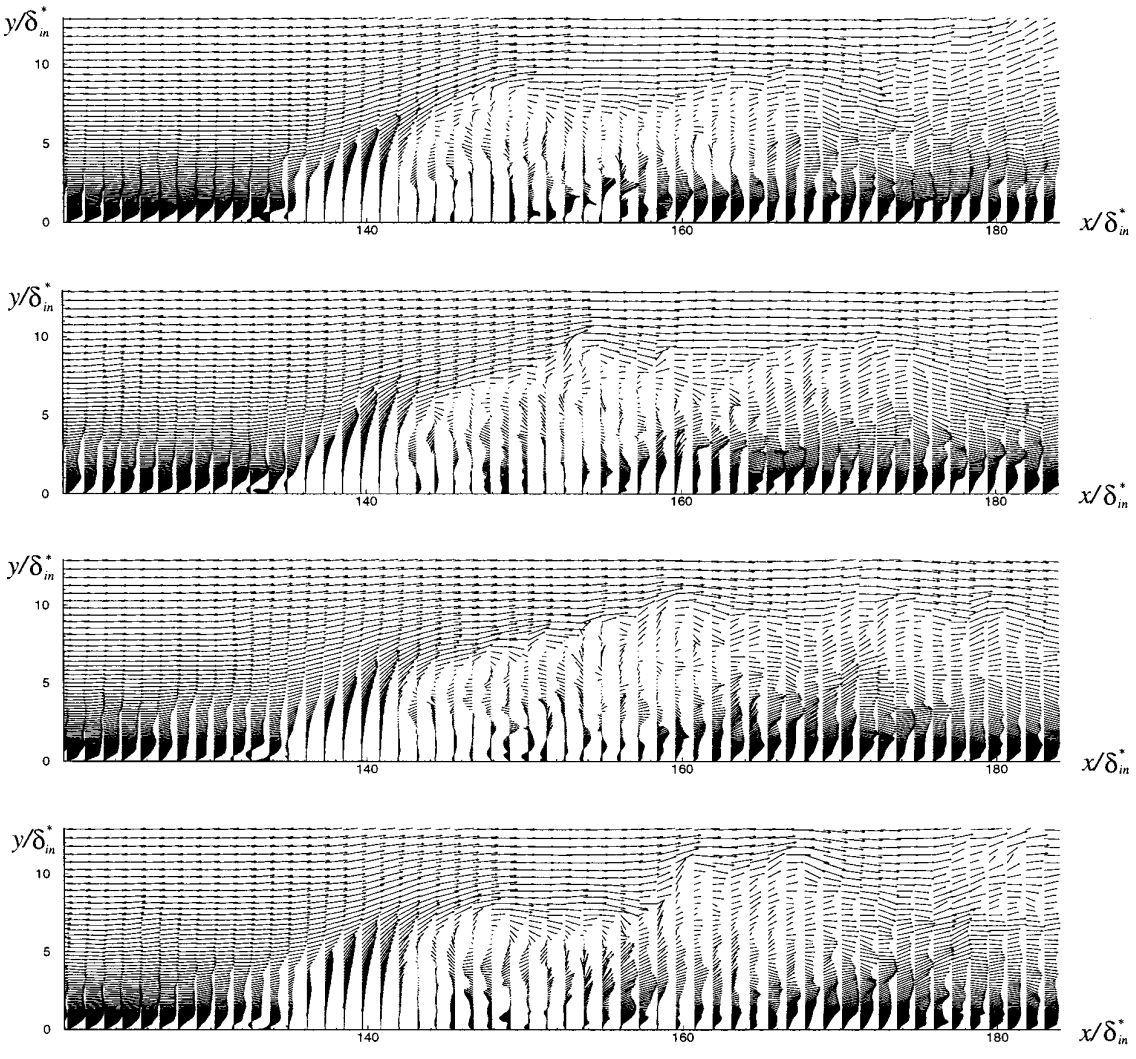

FIG. 11. Time sequence of the flow field (u, v) in the center plane (x, y). Time interval in consecutive plots is $10\delta^*_{\text{in}}/u_\infty$.

Small scales are generated near the hole due to the complex turbulent motion there and thus streaky structures are completely destroyed. Streaky structures are almost recovered at the exit of the flow.

Figure 14 shows contours of the streamwise vorticity in the (z, y) planes. Strong near-wall streamwise vortices are observed at $1d$ and $2d$ upstream locations from the hole, which is characteristic of the fully developed turbulent boundary layer flow (Figs. 14a and b). Injection from the hole lifts up the streamwise vortices (Fig. 14c) above the wall and thus strong vortices are observed around $y/\delta^*_{\text{in}} \approx 3$ right above the injection hole. Also, small scale vortices are observed near the sides of the hole. The lifted vortices and vortex shedding due to the jet create small scales above the wall at the further downstream (Figs. 14d and e). At the far downstream of the hole (Fig. 14f) the vortices reattach to the wall and turbulent boundary layer flow redevelops. A similar behavior was also observed in a turbulent boundary layer with separation [15].

Figure 15 shows the mean secondary flow $(\overline{v}, \overline{w})$ above the wall. It clearly shows that a mean streamwise vortex pair (so-called kidney vortices) exists in the downstream of the jet and plays an important role in the dynamics of the jets in a cross flow. As the flow marches downstream, the strength of this vortex pair gets weaker and the center of this vortex pair moves away from the wall, implying that the locations of these vortices are closely connected to the passage of the jet ejected from the hole. These vortices entrain fluids towards the wall from the sides and eject them away from the wall at the center plane. On the other hand, the horseshoe vortex existing very near the hole is small and weak, compared to the kidney vortices (see Fig. 15a), and thus is absorbed by the kidney vortices

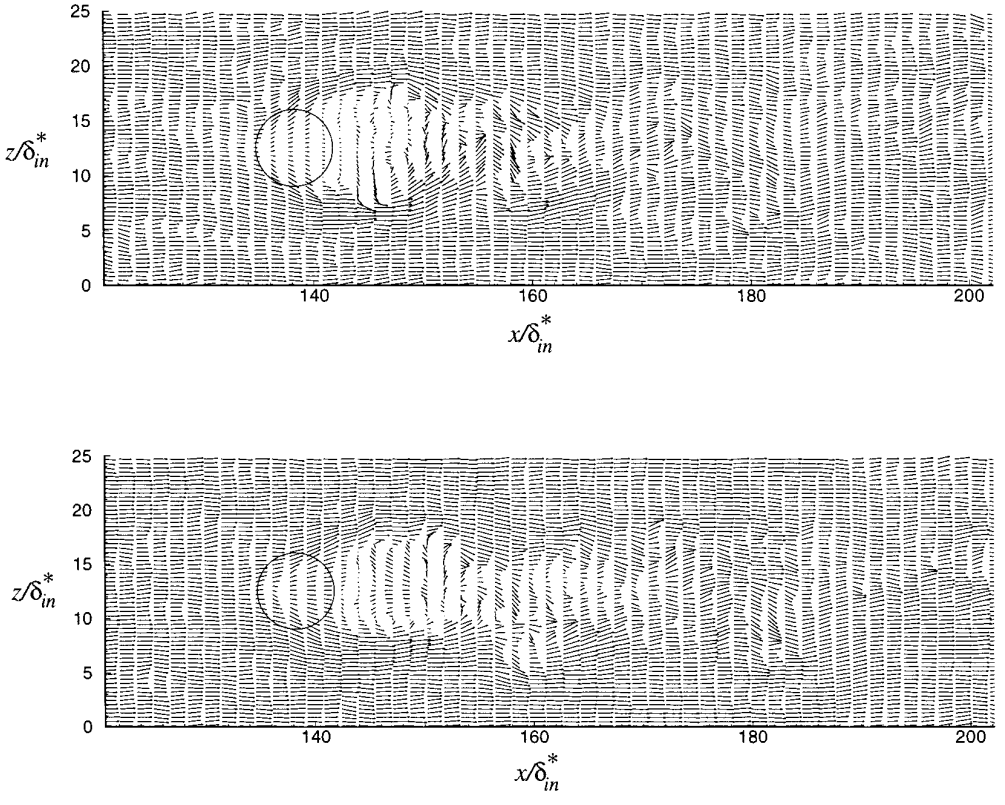

FIG. 12. Velocity vector (u, w) in (x, z) planes: $y/\delta^*_{\text{in}} = 2$ (top); $y/\delta^*_{\text{in}} = 4$ (bottom).

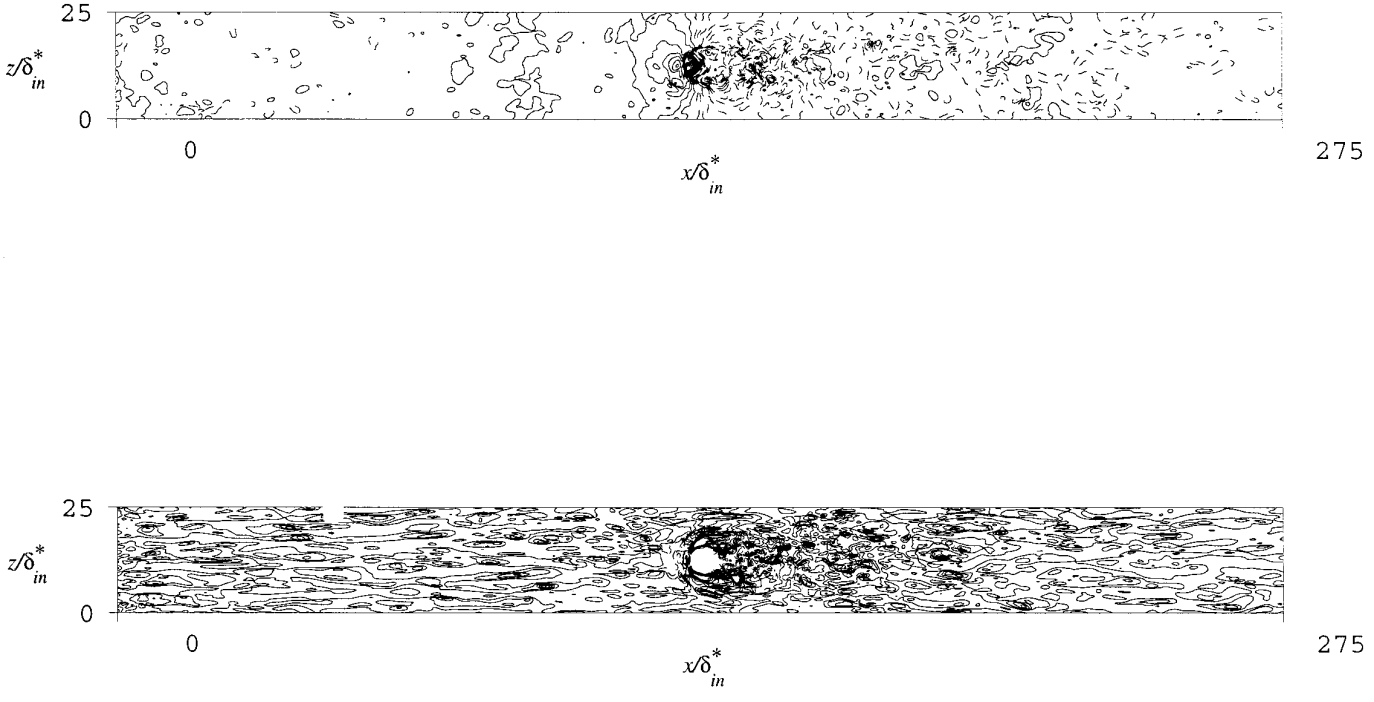

FIG. 13. Contours of the wall pressure (top) and the streamwise velocity at $y = 0.004\delta^*_{\text{in}}$ (bottom).

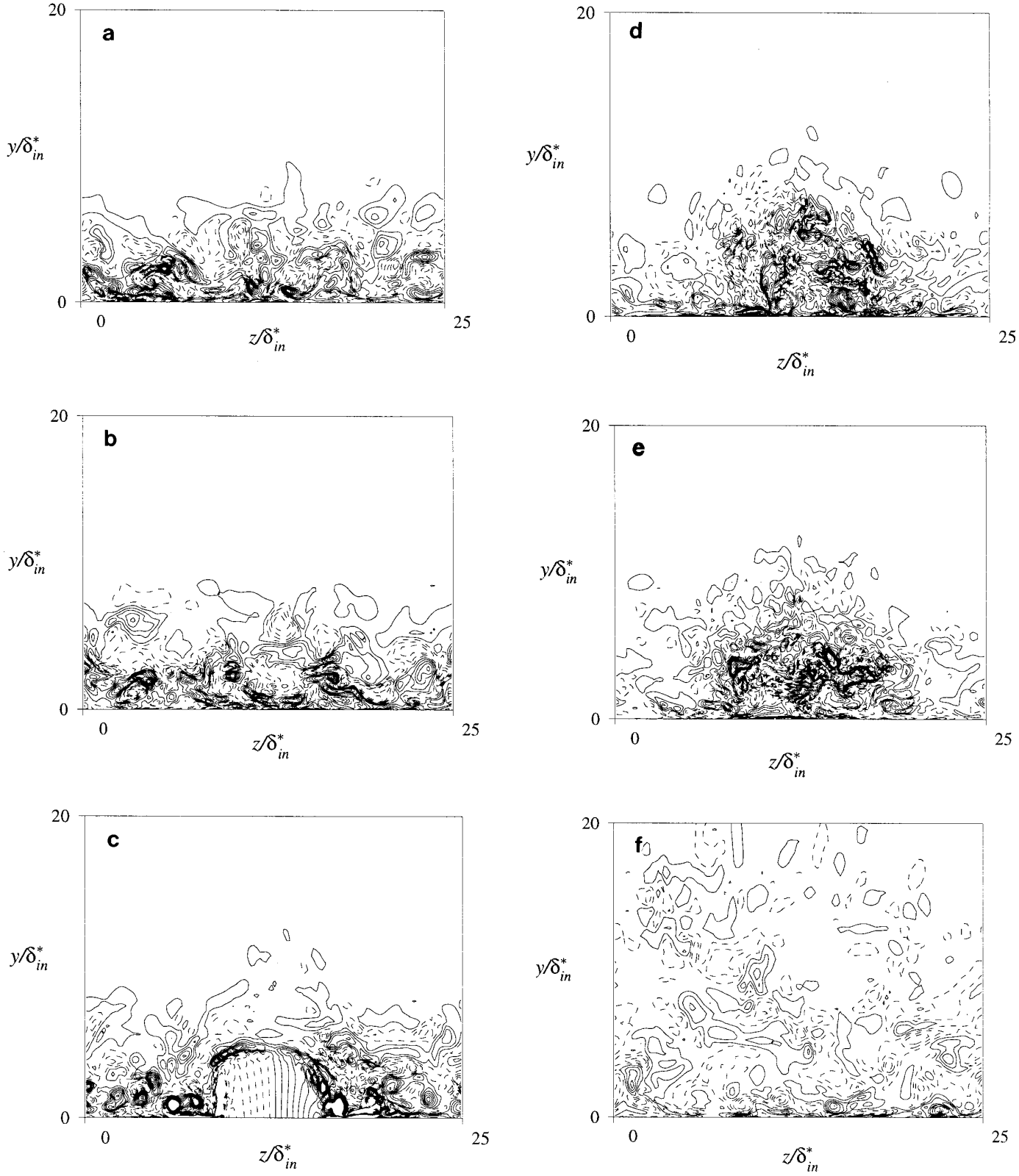

FIG. 14. Contours of the streamwise vorticity in (z, y) planes. The streamwise locations from the hole are (a) 2d upstream; (b) 1d upstream; (c) right above the hole; (d) 1d downstream; (e) 2d downstream; (f) 18d downstream.

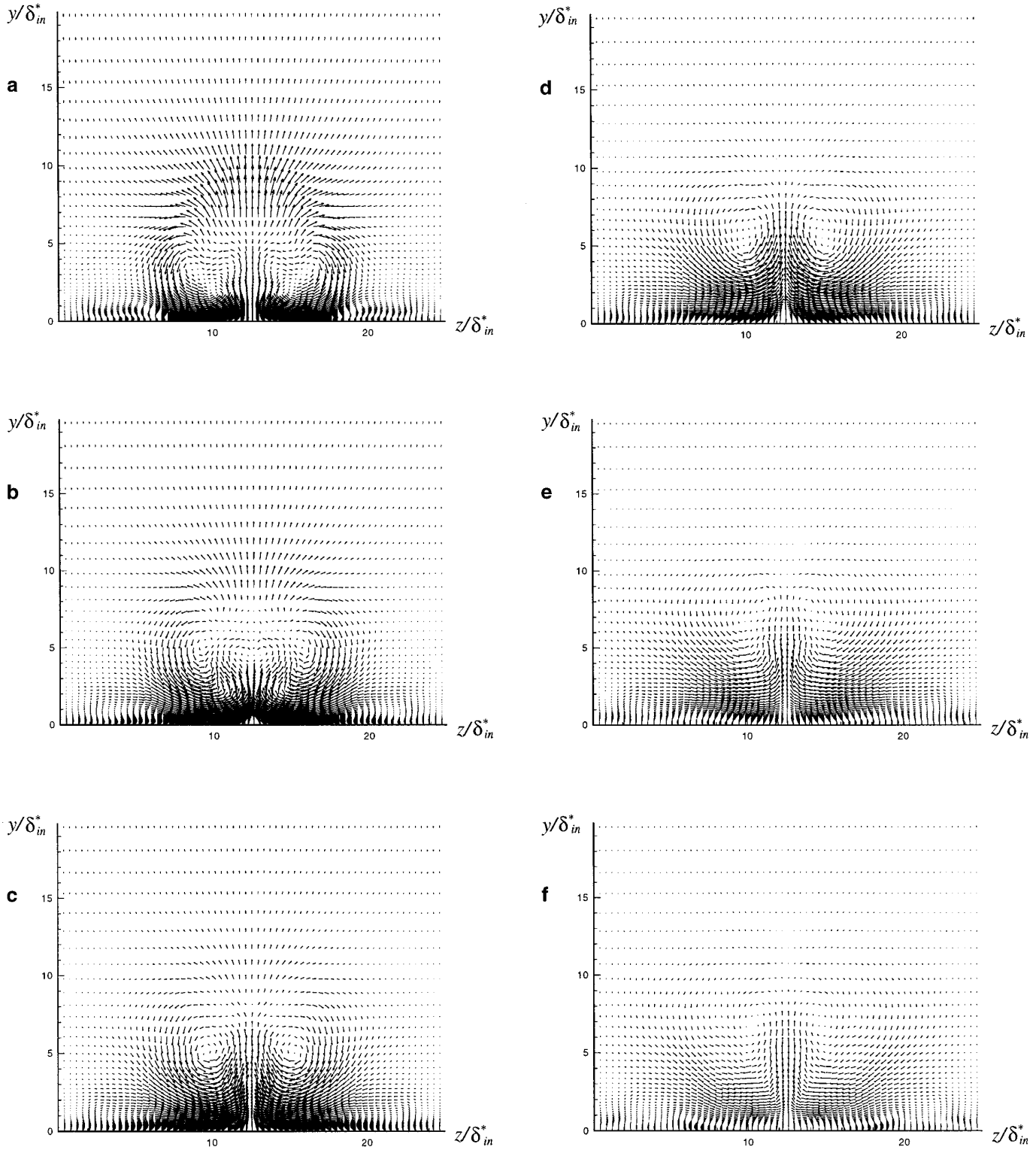

FIG. 15. Mean cross flow in (z, y) planes: (a) $0.5d$ downstream; (b) $1d$ downstream; (c) $1.5d$ downstream; (d) $2d$ downstream; (e) $2.5d$ downstream; (f) $3d$ downstream. The jet locates at $z/\delta^*_{\text{in}} = 8.98 - 16.02$.

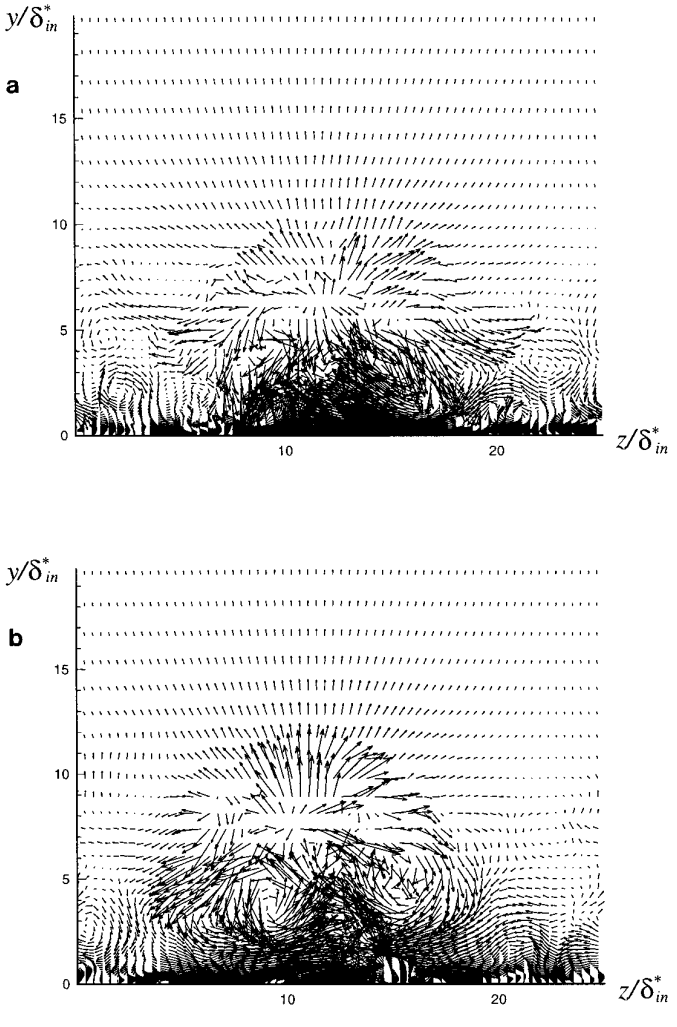

FIG. 16. Instantaneous velocity vector (v, w) at (a) $0.5d$ and (b) $1d$ downstream of the hole. The jet locates at $z/\delta^*_{in} = 8.98 - 16.02$.

downstream. This finding is also reported in [2]. Figure 16 shows instantaneous velocity vectors (v, w) at $0.5d$ and $1d$ downstream of the jet. Note that there exists a clear vortex pair in the instantaneous flow field, which was shown in the long-time averaged mean velocity field (Fig. 15).

5. SUMMARY

Effects of the computational time step and grid stretching on numerical solutions of a laminar boundary layer with a jet injection from the bottom wall were investigated using a fully implicit time advancement scheme. A very large CFL number (CFL = 64) was determined for a time accurate solution, which provided a factor of 50 savings in the required CPU time as compared to a semi-implicit method. Therefore, it was essential to adopt a fully implicit method in simulating the unsteady flow that was caused by jets in a cross flow. It was also noted that the grid stretching generated $2 - \Delta$ waves in the flow investigated.

A full three-dimensional numerical simulation has been performed to qualitatively investigate the interaction of jets in a turbulent cross flow using the direct numerical simulation technique. Turbulent vortex sheddings were observed behind jets and showed a rapid diffusion in the downstream. Near-wall streamwise vortices of the fully developed turbulent boundary layer flow were lifted up and strengthened by the injection from the hole. It was also shown that a counter-rotating vortex pair existing in the downstream of the jet contributed an important role in the dynamics of the jet in a cross flow.

Turbulence statistics of jets in a turbulent cross flow and their energy budgets are being computed and will be reported in the near future. This task requires an enormous amount of time averaging because there is no homogeneous direction in this flow.

ACKNOWLEDGMENTS

This work is sponsored by the Korea Science and Engineering Foundation under Contract No. 95-0200-12-01-3 and by Cray Research, Inc. The use of the supercomputer facilities at the Systems Engineering Research Institute is appreciated. The authors are grateful to Dr. Yang Na for the help in setting up the inflow generation technique during the course of this work.

REFERENCES

1. S. Yavuzkurt, R. J. Moffat, and W. M. Kays, *J. Fluid Mech.* **101,** 129 (1980).
2. J. Andreopoulos and W. Rodi, *J. Fluid Mech.* **138,** 93 (1984).
3. J. H. Leylek and R. D. Zerkle, *J. Turbomach.* **116,** 358 (1994).
4. L. L. Pauley, P. Moin, and W. C. Reynolds, *J. Fluid Mech.* **220,** 397 (1990).
5. H. Choi and P. Moin, *J. Comput. Phys.* **113,** 1 (1994).
6. J. Kim and P. Moin, *J. Comput. Phys.* **59,** 308 (1985).
7. R. M. Beam and R. F. Warming, *J. Comput. Phys.* **22,** 87 (1976).
8. P. M. Gresho and R. L. Lee, *Comput. & Fluids* **9,** 223 (1981).
9. W. Shyy, M.-H. Chen, R. Mittal, and H. S. Udaykumar, *J. Comput. Phys.* **102,** 49 (1992).
10. A. B. Cain and R. H. Bush, *AIAA-94-0172,* 1994.
11. S. K. Robinson, The kinematics of turbulent boundary layer structure, *NASA TM 103859,* 1991.
12. B. P. Leonard, *Comput. Meth. Appl. Mech. Engrg.* **19,** 59 (1979).
13. M. M. Rai and P. Moin, *J. Comput. Phys.* **96,** 15 (1991).
14. P. R. Spalart, *J. Fluid Mech.* **187,** 61 (1988).
15. Y. Na and P. Moin, Direct numerical simulation of turbulent boundary layers with adverse pressure gradient and separation, *Report No. TF-68,* Thermosciences Division, Dept. of Mechanical Eng., Stanford University, 1996.
16. H. Le and P. Moin, Direct numerical simulation of turbulent flow over a backward-facing step, *Report No. TF-58,* Thermosciences Division, Dept. of Mechanical Eng., Stanford University, 1995.